ACS OMEGA

Open Access

http://pubs.acs.org/journal/acsodf

Article

Morphology-Driven Bifunctional Activity of Layered Birnessite-Based Materials toward Oxygen Electrocatalysis

Rajesh K. Behera, Alaka P. Sahoo, Debidutta Das, Amarendra Nayak, Sikha Sayantani, Debasis Jena, Swarna P. Mantry, and Kumar S. K. Varadwaj*

Cite This: *ACS Omega* 2025, 10, 4248−4260

Read Online

ACCESS | Metrics & More | Article Recommendations | Supporting Information

ABSTRACT: The chemical, structural, and morphological diversity of birnessite, a 2D layered MnO_2, has opened avenues for its application as an electrocatalyst toward both the oxygen reduction reaction (ORR) and the oxygen evolution reaction (OER). Among pristine birnessites prepared by different methods, the freestanding flakes (primary structure) obtained from molten salt (MS-KMnO) showed remarkable bifunctional activity as compared to samples with thicker plates or a hierarchical honeycomb-like (type-I secondary structure) morphology. While the ORR onset potential (E_{onset}) and halfwave potential ($E_{1/2}$) for MS-KMnO were recorded at 0.89 and 0.81 V vs RHE, respectively, the OER overpotential (η) was found to be 300 mV. We demonstrated heat-induced secondary structure evolution by modification of the molten salt method, which led to a decrease in activity. In contrast to previous studies, the Co-doped birnessite (Co-KMnO) prepared in molten salt showed lower bifunctional activity (ORR, $E_{1/2}$ = 0.72 V; OER, η= 460 mV) as compared to MS-KMnO. Co-KMnO showed an interwoven wrinkled sheet-like (type-II secondary structure) morphology, with Co^{3+} present in both the in-layer and the interlayer. However, in Co-KMnO/360 prepared at a lower reaction temperature, the areal coverage of the type-II structure reduces, leading to an increase in ORR ($E_{1/2}$ = 0.76 V) and OER (η = 440 mV) activity. The chronopotentiometry for 100 h at a constant OER current of 50 mA cm^{-2} showed an increase in potential from 1.62 to 1.89 V and the characterization of the sample post-treatment showed degradation of the layered structure in MS-KMnO. The samples obtained after 1000 CV cycles in both the ORR and the OER regions showed the formation of secondary structures with a substantial decrease in the Mn^{3+}/Mn^{4+} ratio. This study demonstrates that morphology tuning within the 2D birnessite system has a marked effect on its bifunctional activity.

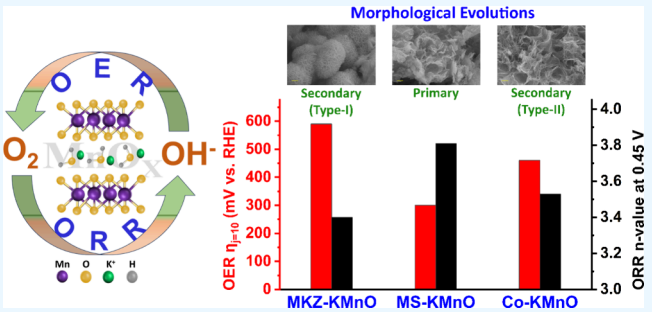

1. INTRODUCTION

The growing dependency on depleting fossil fuels and the serious emission of polluting greenhouse gases have created an urgent need for mankind to develop alternative clean energy sources and efficient energy conversion systems. These systems include fuel cells, metal−air batteries, and electrolyzers, which are expected to play a major role in creating a sustainable energy landscape.[1,2] The two reverse electrochemical reactions, the oxygen reduction reaction (ORR) and the oxygen evolution reaction (OER), including both electron and proton transfer are of utmost importance in technology-driven processes.[3−5] While ORR is the cathodic reaction in the working of fuel cells and the charging of metal−air batteries, OER is the anodic reaction for electrochemical water-splitting.[6,7] The practical application of these energy conversion systems is severely hindered due to the slow kinetics and large thermodynamic overpotential (η) of both ORR and OER, respectively, thus requiring highly efficient and durable electrocatalysts.[8,9] So far, platinum- and palladium-based materials are extensively used as ORR catalysts, while RuO_2 and IrO_2 are recognized as efficient catalysts for OER.[10,11] Although these materials show remarkably high activity, their low earth abundance and serious stability issues keep them from being used as long-term and sustainable catalysts. Therefore, the development of non-noble-metal-based, highly active, and durable bifunctional catalysts made up of earth-abundant elements is one of the core issues to meet the future energy demand.[12] Owing to the high abundance, variable oxidation state, different polymorphs, and low toxicity, manganese oxide (MnO_x)-based materials have gained immense attention for their use as electrocatalysts for both ORR and OER.[13−16] Inspired by nature's oxygen-evolving complex in photosystem II (PS II), which consists of Ca and

Received: June 12, 2024
Revised: November 28, 2024
Accepted: January 23, 2025
Published: February 2, 2025

Mn as metal centers, much progress has been made to replicate this model in artificial photosynthesis.[17,18]

A considerable amount of work has been conducted to synthesize different polymorphs of MnO_2 and study their activities toward ORR and OER. The catalytic performance of MnO_2 strongly depends on the crystal structure, with α-MnO_2 and δ-MnO_2 showing the highest and lowest activities, respectively.[19] Although MnO_2 with various crystal structures has different distinct morphologies, this aspect has not been taken into account while comparing their activities. In particular, while α-MnO_2 takes up 1D nanorod or nanowire forms, a honeycomb-like morphology is observed for δ-MnO_2.[20] Within such diverse polymorphs, birnessite is a layered mixed Mn(III/IV) oxide possessing unique two-dimensional (2D) MnO_2 layers containing different hydrated cations in the interlayer. According to previous reports, birnessite displays nanosheet, nanoflake, or hierarchical honeycomb-like morphologies.[21−23] Birnessite is a moderately active OER catalyst exhibiting an η of nearly 750 mV (at 10 mA cm^{-2}) in alkaline conditions.[19,24−26] To improve the inferior activity, numerous modifications have been made to the birnessite system.

The layered birnessite structure has the flexibility to accept different cations in the interstitial space as well as in the framework position. The ion-exchange process enables the realization of different cations in the interlayer, whereas doping in the framework requires the addition of dopant ions during the synthesis; both are efficient pathways to alter the OER and ORR activities.[26−31] Sun et al. reported enhanced ORR activity of Ce intercalated birnessite, which is attributed to its higher surface area and appearance of the Mn^{3+}/Mn^{4+} redox couple in the voltammogram.[30] In a recent study on birnessite with different alkali metal ions intercalated, enhanced bifunctional activity was observed in Li-birnessite, which was also corroborated by DFT calculations.[31] In one of our studies, MnO_x nanostructures grown on graphene showed enhancement in ORR activity only when the Mn^{3+}/Mn^{4+} redox peaks appear in the cyclic voltammetry (CV) curve.[32] Enhanced ORR activity has also been reported in Cu^{2+}- and Ag^{+}-doped birnessite, where the Ag^{+}-doped sample showed a halfwave potential ($E_{1/2}$) at 0.80 V vs RHE with an n value of 3.92.[33,34] In a series of studies, different transition metal ions were systematically incorporated into the birnessite lattice and their effect on the OER activity was studied. During intercalation, the Cu^{+} precursor disproportionates to Cu^{0} and Cu^{2+}, and the modified samples showed reduction in charge-transfer resistance (R_{CT}) and enhancement in OER activity, with an η_{OER} value of 490 mV.[24] The intercalation of Co^{2+} and Ni^{2+} substantially enhanced the OER activity of birnessite, with η values of 360 and 400 mV, respectively.[35,36] McKendry et al. doped varying amounts of Co and reported the highest OER activity for the Co/Mn atomic ratio of 1:2 with an η value of 420 mV.[25] In another related work, Co^{3+} was incorporated in the layers and simultaneously Fe^{2+} was intercalated between the layers of birnessite to achieve enhanced OER activity with an η as low as 375 mV.[26] A recent study simultaneously incorporated Fe and Ni into the birnessite lattice to obtain improved bifunctional activity owing to the multivalent nature of the metal ions. The surface area and electrical conductivity also increase on multi-ion doping.[37] Doping not only affects the local environment in the birnessite lattice but also modulates the Mn^{3+}/Mn^{4+} ratio. A spectroelectrochemical study revealed that the stabilization of Mn^{3+} at highly alkaline conditions enhances water oxidation for δ-MnO_2.[38] By using the first principal calculations, Peng et al. showed that in birnessite, easy switching of Mn^{3+} and Mn^{4+} oxidation states through an internal potential state and Mn^{3+}-rich surface is critical for catalytic activity toward OER.[39]

In layered MnO_2, the structure of hydrogen bonding between water molecules trapped in the interlayer region plays a vital role in the electron-transfer process. In a theoretical investigation, Remsingh et al. demonstrated that the ordering of the hydration layer confined between polar sheets leads to frustrated hydrogen bonding, which has a profound effect on ion-surface electron transfer.[40] In a recent experimental investigation on buserite and birnessite with different cations intercalated, the OER activity of birnessite is greater than that of buserite, which is attributed to its lower interlayer distance with enhanced water frustration. Among different studied samples, partially dehydrated Na-birnessite showed the highest activity.[41] In a similar study, increased OER activity was reported for thermally annealed Ni-birnessite and Ni−Mn LDH, with η values of 362 and 383 mV, respectively.[42] Electrodeposited MnO_x films showed enhanced OER activity in an acidic medium (pH 2.5) by potential cycling protocols. This study showed that electrodeposited birnessite such as MnO_x transforms into $Mn(OH)_2$ and Mn_3O_4 at the cathodic potential, which on subsequent anodic conditioning produces a disordered birnessite-like phase with high OER activity.[43] This spinel-to-layer transformation was studied by Li et al. using a stochastic surface walking pathway sampling method, which showed that the transient $H_{0.5}MnO_2$ is the precursor of transition. The spinel-to-layer transition is accompanied by Mn dissolution, dislocation, layer-breaking, and insertion of water/cations in between them.[44]

The oxygen defects generated by plasma etching in K-birnessite remarkably enhanced the OER activity with an η of 240 mV.[28] In another work, improved bifunctional activity was demonstrated in defect- and K^{+}-rich layered MnO_2 due to a synergistic effect. The defects generated vacant Mn coordination sites, which are supposed to facilitate their catalytic activity.[21] Preparation of heterostructures with layered MnO_2 is another research direction to improve its activity. He et al. adopted a partial oxidation method to grow δ-MnO_2 nanoflakes on the surface of octahedral-shaped Mn_3O_4 nanocrystals, which displayed improved ORR activity compared to their individual constituents.[45] Monomolecular δ-MnO_2 was anchored to multiwalled carbon nanotubes (δ-MnO_2@MWCNTs), which showed improved ORR activity due to the dominant (002) facet and abundant oxygen vacancies of the δ-MnO_2 layer. The easy adsorption of the O_2 molecule and elongation of O−O bond accelerates the oxygen reduction activity.[46] A sandwich-type composite prepared by the reassembly of birnessite layers and metalloporphyrin (MnTAPP) exhibited OER activity with an η value of 450 mV and a Tafel slope of 230 mV dec^{-1} in an alkaline medium.[47]

The above-discussed studies provide extensive insights into the crystal structure, electronic behavior, interlayer distance, surface area, Mn^{3+}/Mn^{4+} value, etc., of layered MnO_2-based materials and their effect on the electrocatalytic activity toward ORR and OER. However, none of them have explicitly explored the morphology of the materials in relation to their activities. Birnessite, being a 2D layered material, is supposed to exhibit different thicknesses, on the one hand, by the stacking of varying numbers of layers, and, on the other hand,

https://doi.org/10.1021/acsomega.4c05500
ACS Omega 2025, 10, 4248−4260

the layers may fold or entangle to form secondary structures such as nanoflower or honeycombs. The structural evolution of these secondary morphologies in birnessite and the dependence of bifunctional activity on morphology is yet to be explored.

Herein, birnessite is prepared by different reported methods, and their ORR and OER activities are studied along with their morphology. Birnessite prepared by the molten salt method (MS-KMnO) displayed the highest bifunctional activity along with a unique thin freestanding flake-like morphology (primary structures). We demonstrated a heat-induced transition of primary structures into a hierarchical honeycomb-like type-I secondary structure through the exothermic decomposition of glucose at the same reaction temperature. Such changes in morphology are accompanied by a decrease in activity. We also prepared Co-doped birnessite in molten salt at varying temperatures, which, in contrast to earlier studies, showed a decrease in activity as compared to their pristine counterpart, which may be correlated to a type-II secondary structure. Furthermore, the preparation of Co-doped samples at lower temperatures showed a remarkable decrease in the density of the type-II morphology accompanied by an increase in activity.

2. EXPERIMENTAL SECTION

2.1. Chemicals and Reagents. All chemicals were of analytical grade and used without further purification. KNO_3, D-glucose, and $MnSO_4.H_2O$ were obtained from Thermo Fisher Scientific India Pvt. Ltd. $Mn(NO_3)_2{\cdot}4H_2O$, $CoCl_2{\cdot}6H_2O$, and Nafion (5% by weight in alcohol) were obtained from Sigma-Aldrich. Concentrated HCl and $KMnO_4$ were purchased from Rankem (Avantor Performance Materials India Ltd.). KOH was purchased from Sisco Research Laboratories Pvt. Ltd. Double-distilled (DD) water was used in all experiments.

2.2. Material Synthesis. Birnessite was prepared by four different methods, i.e., molten salt (MS-KMnO), McKenzie's (MKZ-KMnO), sol−gel (SG-KMnO), and hydrothermal (HT-KMnO), as reported in earlier studies.[22,23,48,49] Molten salt method: 3 g of KNO_3 and 0.2 g of $MnSO_4{\cdot}H_2O$ were ground thoroughly for 20 min in a mortar and pestle. Then, the mixture was transferred to a crucible and kept in a muffle furnace preheated at 380 °C for 10 min. Subsequently, the mixture was quenched at room temperature and water-washed by centrifugation, followed by vacuum drying in a desiccator.[22] Keeping the reaction procedure the same, two other samples were prepared by adding 0.001 and 0.002 g of glucose to the reaction mixture of KNO_3 and $MnSO_4{\cdot}H_2O$. The obtained samples were named G1-KMnO and G2-KMnO, respectively. Cobalt-doped birnessite samples were prepared by the addition of 0.12 g of $CoCl_2{\cdot}6H_2O$ to the reaction mixture of KNO_3 and $MnSO_4{\cdot}H_2O$. The samples were prepared by heating the reaction mixture at 380 °C (Co-KMnO), 370 °C (Co-KMnO/370), and 360 °C (Co-KMnO/360). Other reaction parameters remained unchanged. McKenzie's method: 50 mL of 4 M HCl was added dropwise to 250 mL of 0.2 M $KMnO_4$ solution at 80 °C. The sample was stirred for another 30 min at 80 °C followed by 50 °C for 15 h. After completion of the reaction, the sample was vacuum-filtered, washed, and dried.[48] Sol−gel method: 50 mL of 0.38 M $KMnO_4$ was added to 20 mL of 1.4 M D-glucose solution. On shaking, an exothermic reaction was initiated with gel formation. The sample was left undisturbed, allowed to cool down for 30 min, and dried overnight at 110 °C. The gel was calcinated at 400 °C for 2 h, water-washed, and dried at 110 °C.[49] Hydrothermal method: 3.58 g of $Mn(NO_3)_2{\cdot}4H_2O$ was added to 40 mL of DD water followed by an addition of 3.16 g of $KMnO_4$ under constant stirring. The solution was transferred to a Teflon bottle and sealed in a stainless steel autoclave. The autoclave was kept in an oven at 50 °C for 48 h. After cooling down to room temperature, the sample was water-washed and dried under an infrared (IR) lamp.[23]

2.3. Materials Characterization. The crystal structure of the powder samples was determined through X-ray diffraction (XRD) by an Ultima IV RIGAKU advance X-ray diffractometer using Cu Kα radiation (λ = 0.154 nm) at a scan rate of 2° min^{-1} at room temperature. The morphology of the synthesized samples was evaluated by field-emission scanning electron microscopy (FESEM) using a Zeiss microscope (Gemini SEM 300). Energy-dispersive X-ray spectroscopy (EDS) along with elemental mapping was also carried out using the EDAX element by Ametek Inc. The surface area of the catalyst was determined by the Brunauer−Emmett−Teller method (BET) through N_2 sorption measurements performed using Quantachrome instruments AutosorbiQ-XR at 77 K. The surface elemental composition and their oxidation states for the samples were examined by X-ray photoelectron spectroscopy (XPS) measurements conducted on a PHI 5000 versa probe II instrument with Mg-Kα radiation as the excitation source. Transmission electron microscopy (TEM), high-resolution TEM (HRTEM), and selected area electron diffraction (SAED) images were obtained using a JEOL 2100 plus electron microscope operated at an acceleration voltage of 200 kV. The samples were dispersed in ethanol and drop-cast on a carbon-coated copper grid for TEM measurements. The thickness of the 2D flakes was studied by atomic force microscopy (AFM), using Oxford Instruments MFP-3D Origin AFM. The sample was sonicated in ethanol for 1 h, spin-coated over a KOH-treated glass slide, and studied in the noncontact mode.

2.4. Electrochemical Studies. Electrocatalytic measurements were conducted in a computer-controlled Autolab potentiostat/galvanostat (PGSTAT 204 Metrohm-Autolab B.V., The Netherlands). A glassy carbon electrode (GCE) (3 mm diameter) was used as the working electrode, which was polished properly using 0.05 μm alumina powder and washed thoroughly with DD water to obtain a clean shining surface. Ag/AgCl (3 M KCl) was used as the reference electrode for ORR and Hg/HgO (1 M KOH) for OER, which were calibrated with respect to the reversible hydrogen electrode (RHE). A glassy carbon rod was used as the counter electrode for both ORR and OER studies. All values recorded with the reference electrodes were later converted to the RHE (Figure S1a,b).

Three types of inks were prepared for specific electrochemical studies. For ORR, the catalyst ink (Ink-1) was prepared as follows: 1 mg of catalyst and 1 mg of Vulcan carbon (Vulcan XC-72) were mixed in 1.6 mL of DD water, 0.4 mL of isopropanol, and 10 μL of Nafion solution. Then, the solution was sonicated for 15 min to obtain a homogeneous mixture of the catalyst ink. For comparison, ink preparation for 20% Pt/C was performed without adding Vulcan carbon. 12 μL of the catalyst ink was then loaded on the GCE (3 mm diameter) and kept in a desiccator for drying. This ink was used for CV, rotating disk electrode (RDE), rotating ring disk electrode (RRDE), double-layer capacitance

https://doi.org/10.1021/acsomega.4c05500
ACS Omega 2025, 10, 4248−4260

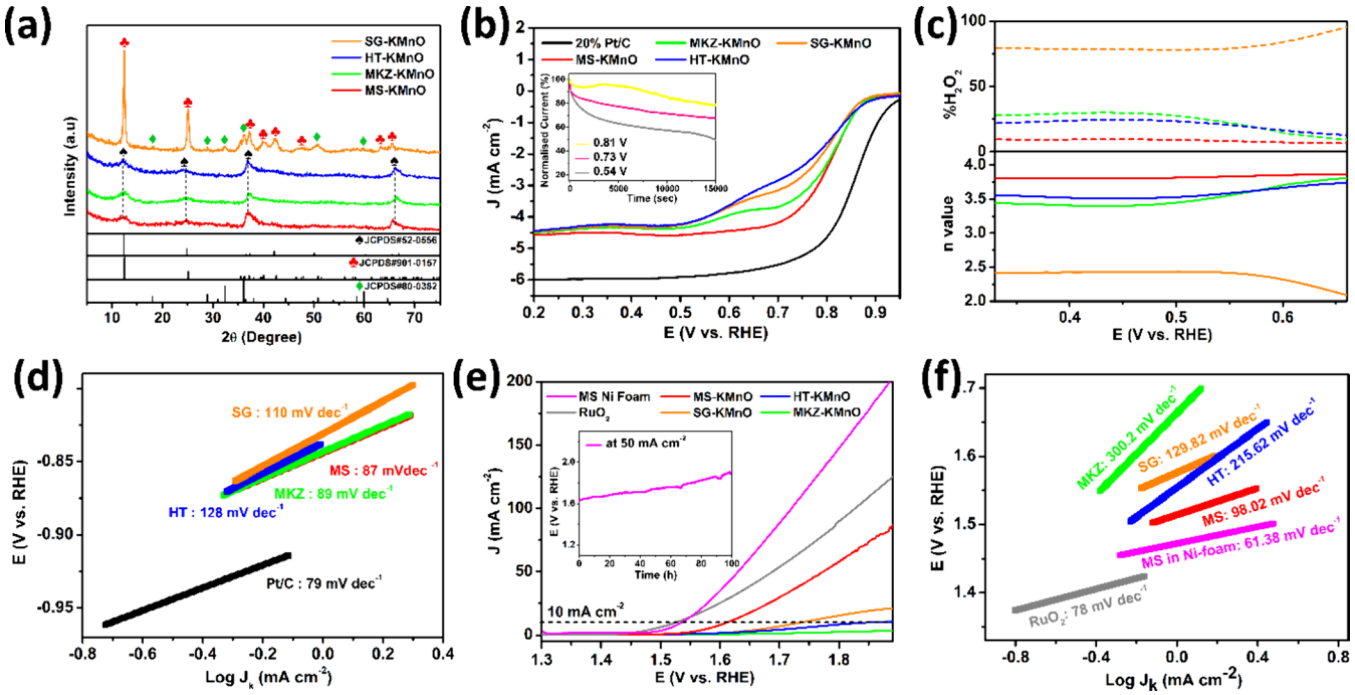

Figure 1. (a) XRD patterns and (b) RDE polarization curves for ORR of the samples prepared by four different methods; (inset of (b)) chronoamperometric studies for MS-KMnO at 0.81, 0.73, and 0.54 V. The yellow, pink, and gray lines represent 0.81, 0.73, and 0.54 V potentials, respectively. (c) The $\%H_2O_2$ and n values as calculated from the RRDE curves (the red, green, blue, and orange lines represent MS-KMnO, MKZ-KMnO, HT-KMnO, and SG-KMnO samples, respectively). (d) Tafel plots for ORR. (e) OER polarization curves of MS-KMnO measured in Ni foam (magenta) and the samples prepared by the four methods along with RuO_2; (inset of (e)) chronopotentiometric studies for MS-KMnO at 50 mA cm^{-2} for 100 h. (f) Tafel plots for OER.

(C_{dl}), electrochemical impedance spectroscopy (EIS), and chronoamperometric tests.

For OER, the catalyst ink (Ink-2) was prepared as follows: 4 mg of catalyst and 4 mg of Vulcan carbon were mixed in 1.6 mL of DD water, 0.4 mL of isopropanol, and 8 μL of Nafion solution. Then, the solution was sonicated for 30 min to obtain a homogeneous mixture of the catalyst ink. Ink preparation of RuO_2 was performed without adding Vulcan carbon. Then, 5 μL of the catalyst ink was loaded onto the GCE (3 mm diameter). The GCE was kept in a desiccator for drying. This ink was used only for RDE studies toward OER.

In the case of chronopotentiometry for the OER, the catalyst ink (Ink-3) was prepared as follows: 2 mg of catalyst was added to 0.4 mL of isopropanol and 0.4 mL of Nafion solution. The mixture was then ultrasonicated for 60 min to obtain a homogeneous dispersion. The ink was then drop-cast onto clean Ni foam of 1 cm^2 area.

Initially, CV was performed in the ORR potential range of 0 to −0.8 V (vs Ag/AgCl) at 10, 50, and 100 mV s^{-1} scan rates in N_2-saturated (for 30 min) 0.1 M KOH. Then, the same electrolyte was saturated with O_2 (for 30 min) and CV was performed at the same scan rates and potential range.

For linear sweep voltammetry (LSV) measurements, the KOH electrolyte solution was first saturated with aqueous O_2 for 30 min followed by RDE measurements. For ORR, 0.1 M KOH was used in the potential range of 0 to −0.8 V (vs Ag/AgCl) at a scan rate of 10 mV s^{-1}. In the case of OER, 1 M KOH was used in the potential range of 0.3 to 1.0 V (vs Hg/HgO) at a scan rate of 5 mV s^{-1}. The rotation speed of the electrode in both cases was set at 1600 rpm.

For RRDE studies, 20 μL of catalyst ink was drop-casted on GCE (5 mm diameter). Electrochemical measurements were executed in the ORR potential range 0 to −0.8 V (vs Ag/AgCl) in 0.1 M KOH electrolyte at 1600 rpm. The potential of the Pt ring was fixed at 1.52 V vs RHE. RRDE was used to evaluate the performance of the catalyst in terms of peroxide yield ($\%H_2O_2$) and electron transfer number (n) by using eq 1 and 2, respectively:

$$\%H_2O_2 = 200 \times \frac{I_R/N}{I_D + I_R/N} \quad (1)$$

$$n = 4 \times \frac{I_D}{I_D + I_R/N} \quad (2)$$

where I_D and I_R are the disk and ring current, respectively, and the collection efficiency (N) is 0.25 for the Pt ring.

The electrochemically active surface area (ECSA) has a linear proportional relationship with the double-layer capacitance (C_{dl}) value. First, CV was performed in the potential range of 0.07−0.17 V (vs Ag/AgCl) at 20, 30, 40, and 50 mV s^{-1} in N_2-saturated 0.1 M KOH. The C_{dl} values were then obtained from the plot between the difference in current density ($\Delta J = J_a - J_c$) vs scan rate. EIS tests were performed on a CHI 660A electrochemical workstation in an O_2-saturated 0.1 M KOH electrolyte. The frequency range was 10^{-2}−10^5 Hz at 0.76 V potential.

Chronoamperometry studies for ORR were performed with the same three-electrode cell in O_2-saturated 0.1 M KOH, and a continuous flow of O_2 was maintained throughout the process. The working electrode was rotated at 1600 rpm for 15000 s. Chronopotentiometry was performed at 50 mA cm^{-2} in N_2-saturated 1 M KOH for 100 h.

The average oxidation state was calculated from the ΔE value obtained from the Mn 3s spectra using eq 3

https://doi.org/10.1021/acsomega.4c05500
ACS Omega 2025, 10, 4248−4260

$$AOS = 8.956 - 1.126 \cdot \Delta E_b \quad (3)$$

where ΔE_b is the difference between the orbital binding energies.[50]

3. RESULTS AND DISCUSSION

Figure 1a shows identical XRD patterns for MS-KMnO, MKZ-KMnO, and HT-KMnO having diffraction peaks at d-values of 7.0 (12.6°), 3.6 (25°), 2.4 (36.9°), and 1.4 Å (65.9°), which may be assigned to the (003), (006), (012), and (110) planes, respectively, for layered manganese oxide with a rhombohedral structure (ref card no. #52-0556). Higher-intensity diffraction lines depict the higher crystallinity of SG-KMnO. The diffraction peaks for SG-KMnO at 7.0 (12.5°), 3.54 (25.1°), 2.41 (37.2°), 2.26 (39.7°), 2.12 (42.5°), 1.46 (63.5°), and 1.42 Å (65.4°) match with the (001), (002), ($\bar{1}$01), (012), (112), (121), and ($\bar{1}$12) planes of birnessite (ref card no. # 96-901-0157) and peaks at 4.9 (17.9°), 3.08 (28.8°), 2.76 (32.4°), 1.79 (50.6°), and 1.54 Å (59.6°) match with the (101), (112), (103), (105), and (224) planes of Mn_3O_4 (JCPDS #80-0382), respectively.[49]

CV curves for the samples (Figure S2) show a distinct reduction current in the O_2-saturated solution, confirming their catalytic activity toward ORR. The reduction peaks for MS-KMnO, MKZ-KMnO, HT-KMnO, and SG-KMnO are observed at 0.78, 0.61, 0.63, and 0.70 V, respectively. The RDE polarization curves in Figure 1b show the E_{onset} and $E_{1/2}$ values for MS-KMnO, MKZ-KMnO, HT-KMnO, and SG-KMnO at (0.89, 0.81 V), (0.88, 0.80 V), (0.89, 0.77 V), and (0.87, 0.78 V), respectively (Table S1). At higher negative potentials, the current saturates to 4.57 mA cm^{-2} for MS-KMnO. The substantially more positive CV peak potential, E_{onset}, $E_{1/2}$, and higher J_L for MS-KMnO among the studied samples demonstrate its higher efficiency toward ORR. The I_D and I_R curves in the RRDE studies (Figure S3) led to the estimation of the n value and amount of H_2O_2 yield, as depicted in Figure 1c. At 0.45 V, the n values for MS-KMnO, MKZ-KMnO, HT-KMnO, and SG-KMnO are found to be 3.81, 3.4, 3.51, and 2.43, respectively. The corresponding amounts of H_2O_2 generation are 9.7, 29.9, 24.5, and 78.5%, respectively. The highest n value and lowest $\%H_2O_2$ demonstrate the superior ORR activity of MS-KMnO. More insight into the ORR kinetics is obtained from the Tafel plots for different catalysts as derived from their corresponding LSV curves (Figure 1d). The Tafel slope for MS-KMnO is 87 mV dec^{-1}, which is the lowest among the birnessite samples. The Tafel slopes for 20% Pt/C, MKZ-KMnO, SG-KMnO, and HT-KMnO are 79, 89, 110, and 128 mV dec^{-1}, respectively. ECSA is estimated in terms of C_{dl} calculated from the current density difference vs the scan rate plot (Figure S4). The background noise dominates the CV curves because of the low non-faradic current for MKZ-KMnO, HT-KMnO, and SG-KMnO, which remains unchanged after 100 CV cycles. The C_{dl} values for MS-KMnO, MKZ-KMnO, HT-KMnO, and SG-KMnO are 13.53, 4.48, 1.79, and 1.25 mF cm^{-2}, respectively. The highest C_{dl} value for MS-KMnO implies a greater ECSA and superior activity.

RDE polarization curves (Figure 1e) were obtained through an anodic scan up to 1.9 V vs RHE to evaluate the OER activity. MS-KMnO shows substantially enhanced activity with a current density of 10 mA cm^{-2} achieved at 1.61 V vs RHE ($E_{j=10}$). The $E_{j=10}$ for SG-KMnO is 1.74 V, while MKZ-KMnO and HT-KMnO did not exhibit any measurable activity (Table S2). The Tafel slope for MS-KMnO (98 mV dec^{-1}) is comparable to that of RuO_2 (78 mV dec^{-1}), demonstrating its excellent activity (Figure 1f). Subsequently, the Tafel slopes for MKZ-KMnO, SG-KMnO, and HT-KMnO are 300, 130, and 216 mV dec^{-1}, respectively. In recent studies, K-birnessite prepared by the redox solution-phase method and loaded on Ni foam showed $E_{j=10}$ at 1.61 V.[28,29] In comparison, the OER activity of MS-KMnO (ink-3 without VC) loaded on Ni foam showed $E_{j=10}$ at 1.53 V, which is 80 mV more negative. The Tafel slope of MS-KMnO (Ni foam) of 61 mV dec^{-1} is substantially lower than that of recently reported K-birnessite (106 mV dec^{-1}).[28,29] The OER mechanism in view of the lower Tafel slope value is discussed later.

One of the previous studies on different polymorphs of MnO_2 showed the highest OER activity of α-MnO_2 with an $E_{j=10}$ of 1.73 V and a Tafel slope of 87 mV dec^{-1}.[19] However, the lower $E_{j=10}$ (1.61 V) of MS-KMnO indicates the superior OER activity of molten salt birnessite over other pristine MnO_2 polymorphs. At this point, it may be inferred that the birnessite samples prepared by different methods but depicting identical XRD patterns and crystallinity differ markedly in their bifunctional activity.

The SEM micrographs in Figure 2a–d show distinctly different morphologies of the samples. MS-KMnO comprises randomly distributed freestanding layers (Figure 2a) in which the curled edges demonstrate the low thickness of these 2D sheets. On the other hand, in Figure 2b,c, HT-KMnO and

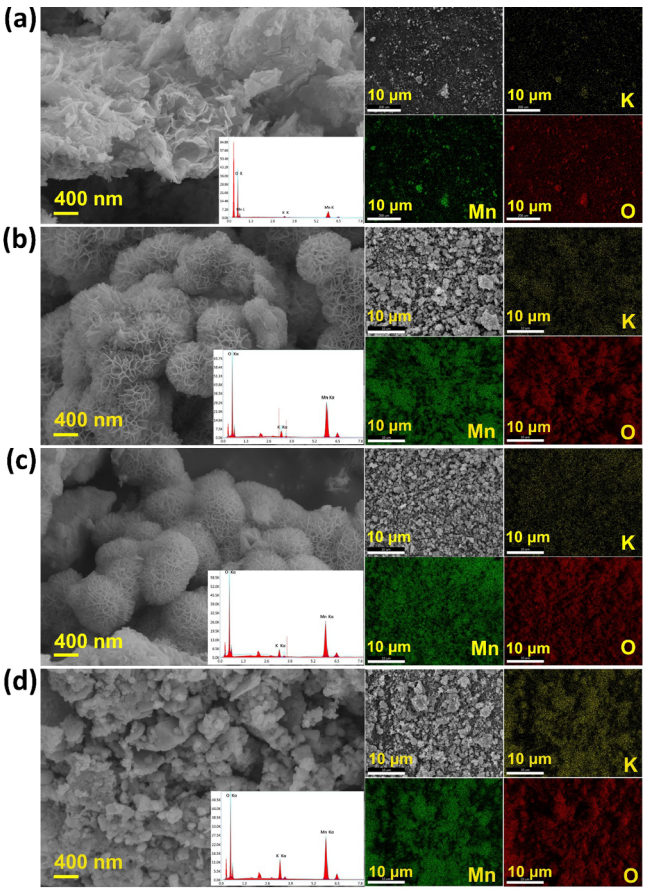

Figure 2. FESEM images at two different magnifications along with EDS spectrum and elemental mapping for (a) MS-KMnO, (b) HT-KMnO, (c) MKZ-KMnO, and (d) SG-KMnO.

https://doi.org/10.1021/acsomega.4c05500
ACS Omega 2025, 10, 4248−4260

MKZ-KMnO show honeycomb-like structures, made up of polygonal voids of different sizes ranging from 50 to 150 nm.[21,23] In the case of SG-KMnO, a thick plate-like morphology is observed (Figure 2d). The EDS spectra for all samples show the presence of Mn, O, and K, and the elemental mapping illustrates their uniform distribution in a broad area. The TEM image of MS-KMnO in Figure 3a shows transparent

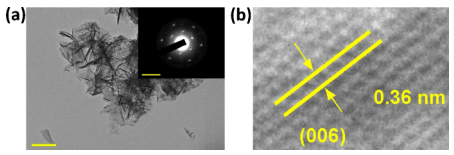

Figure 3. (a) TEM image for MS-KMnO (scale bar, 200 nm); inset depicts its SAED pattern (scale bar 5 1/nm). (b) HRTEM image of MS-KMnO.

sheets of a few hundred nanometers in length. The HRTEM micrograph (Figure 3b) shows the lattice fringes with an interplanar spacing of 0.36 nm, corresponding to the (006) planes of birnessite. The SAED spot pattern (inset of Figure 3a) shows that the 2D sheets in MS-KMnO are single crystalline. The AFM image in Figure S5 depicts isolated 2D flakes of MS-KMnO. The height profile studies for several such flakes showed the lowest thickness of 8 nm representing the thickness of a single flake. In birnessite, each MnO_6 octahedral layer is 0.7 nm thick, which implies that in MS-KMnO, each thin flake is formed by the stacking of around 10 such layers. Another 2D structure showing 16 nm thickness may be due to the placement of one flake over another.

To understand the morphology evolution in different samples, we propose that the freestanding, few-layer-thick 2D sheets observed in MS-KMnO are metastable in nature. These structures, termed primary structures, stack upon each other to form thicker layers. However, in another course of development, the edges and certain positions along the layer surface may join to create stable polygonal voids, which assemble to form higher-order spherical or elliptical shapes. This hierarchy with honeycomb-like morphology is named a type-I secondary structure.

To experimentally verify this hypothesis, we designed a modified molten salt method in which the reaction is carried out in the presence of different amounts of glucose (0.001 and 0.002 g), keeping all other parameters unchanged. The XRD peaks for G1-KMnO and G2-KMnO in Figure 4a match with that of birnessite, while the peak at 2.76 Å is due to the gradual evolution of the Mn_3O_4 phase (JCPDS #80-0382). SEM micrographs for G1-KMnO and G2-KMnO in Figure 4e,f show a drastic change in morphology compared to that of MS-KMnO. While the honeycomb-like secondary morphology is prominent for G2-KMnO, such features are in a developing stage for G1-KMnO. This demonstrates that the exothermic decomposition of glucose in the molten salt produces the required energy for layer−layer attachment at certain positions, which leads to the formation of a secondary morphology.

The LSV curves in Figure 4b show the ORR activities of G1-KMnO and G2-KMnO as compared to that of MS-KMnO. The E_{onset} and $E_{1/2}$ values for G1-KMnO and G2-KMnO were observed at 0.86, 0.78 V, and 0.86, 0.79 V, respectively. The $E_{1/2}$ for G2-KMnO at 0.79 V is 20 mV negative compared to that of MS-KMnO (0.89 V), and the limiting current density of 4.11 mA cm^{-2} is substantially lower than that of MS-KMnO (4.57 mA cm^{-2}). The RRDE studies (Figure S6) also corroborate the above observations, which show a considerable decrease in the n value to 3.72 and an increase in the $\%H_2O_2$ of 23.3 for G2-KMnO as compared to that of MS-KMnO (n = 3.81, $\%H_2O_2$ = 9.7). The LSV curves for oxygen evolution in Figure 4d show that $E_{j=10}$ for G1-KMnO and G2-KMnO are 1.68 and 1.64 V respectively, which is more positive than that of MS-KMnO (1.61 V, Table S4). This shows that the highest bifunctional activity observed in MS-KMnO among the studied birnessite samples may be attributed to its primary structure with more exposed edge sites, and the formation of secondary structures leads to a decrease in their activity.

In previous studies, the electrocatalytic activity of manganese oxide-based materials is suggested to be affected by the crystal structure, defects, Mn^{3+}/Mn^{4+} ratio, and electronic structure.[19,21,25,38] The incorporation of $Fe^{3+}/Co^{2+}/Ni^{2+}$ in the interlayer region of birnessite has been reported to increase the OER activity. The interlayer reconstruction and the change in the electronic structure with the raising of the valence band caused by dopant ions have been suggested to be the reason for the observed increase in activity.[25,26,28,35,36] Considering the above studies, Co-KMnO was prepared with a synthesis parameter similar to that of MS-KMnO to understand the effect of doping on the morphology and activity, if any. The XRD pattern for Co-KMnO in Figure S7 shows the formation of the birnessite phase, and the crystallinity is higher than that of MS-KMnO.

The polarization curve for Co-KMnO (Figure 5a) shows the ORR activity with E_{onset} and $E_{1/2}$ at 0.84 and 0.72 V, respectively. Compared to MS-KMnO, the E_{onset} and $E_{1/2}$ for Co-KMnO shifts to less positive potentials (ΔE_{onset} = 50 and $\Delta E_{1/2}$ = 90 mV) depicting a decrease in ORR activity on Co doping. It is further substantiated by the lower n value of 3.53 and increased $\%H_2O_2$ yield of 23.3% (Figure S8b) obtained from the RRDE curves of Co-KMnO (Figure S8a). The OER activity of Co-KMnO (Figure 5b) with $E_{j=10}$ at 1.69 V is 80 mV more positive than that of MS-KMnO. The lower ECSA of Co-KMnO (C_{dl} = 3.41 mF cm^{-2}) as compared to that of MS-KMnO (C_{dl} = 13.53 mF cm^{-2}) (Figure S9) further elucidates the decrease in its bifunctional activity. The EIS study for MS-KMnO and Co-KMnO is performed at 0.86 V in the frequency range of 10^{-2}−10^{5} Hz, as shown in Figure S10. The Nyquist plot shows that the diameter of the semicircle is higher in the case of Co-KMnO than that of MS-KMnO, implying a higher charge-transfer resistance (R_{CT}). The bifunctional activity of the Co-doped sample in the present study is substantially lower than that of its pristine counterpart, in contrast to previous studies. To gain more insights into the reason for this reverse trend in activity, morphological analysis was performed.

The SEM images of Co-doped samples depicted in Figures 5c and S11b show a distinct morphology in which thin sheets are interconnected over a broad area under study. Unlike, the type-I secondary structures discussed earlier, the morphological pattern shows thinner layers with curled edges for Co-KMnO. It is neither freestanding as observed in MS-KMnO nor a hierarchical honeycomb-like spherical or elliptical structure, but a different morphology made up of an interwoven network of sheets named a type-II secondary structure. The lower bifunctional activity of Co-KMnO as compared to that of MS-KMnO may be attributed to the formation of this secondary morphology.

The surface area and pore structure of MS-KMnO and Co-KMnO were investigated by N_2 adsorption−desorption

https://doi.org/10.1021/acsomega.4c05500
ACS Omega 2025, 10, 4248−4260

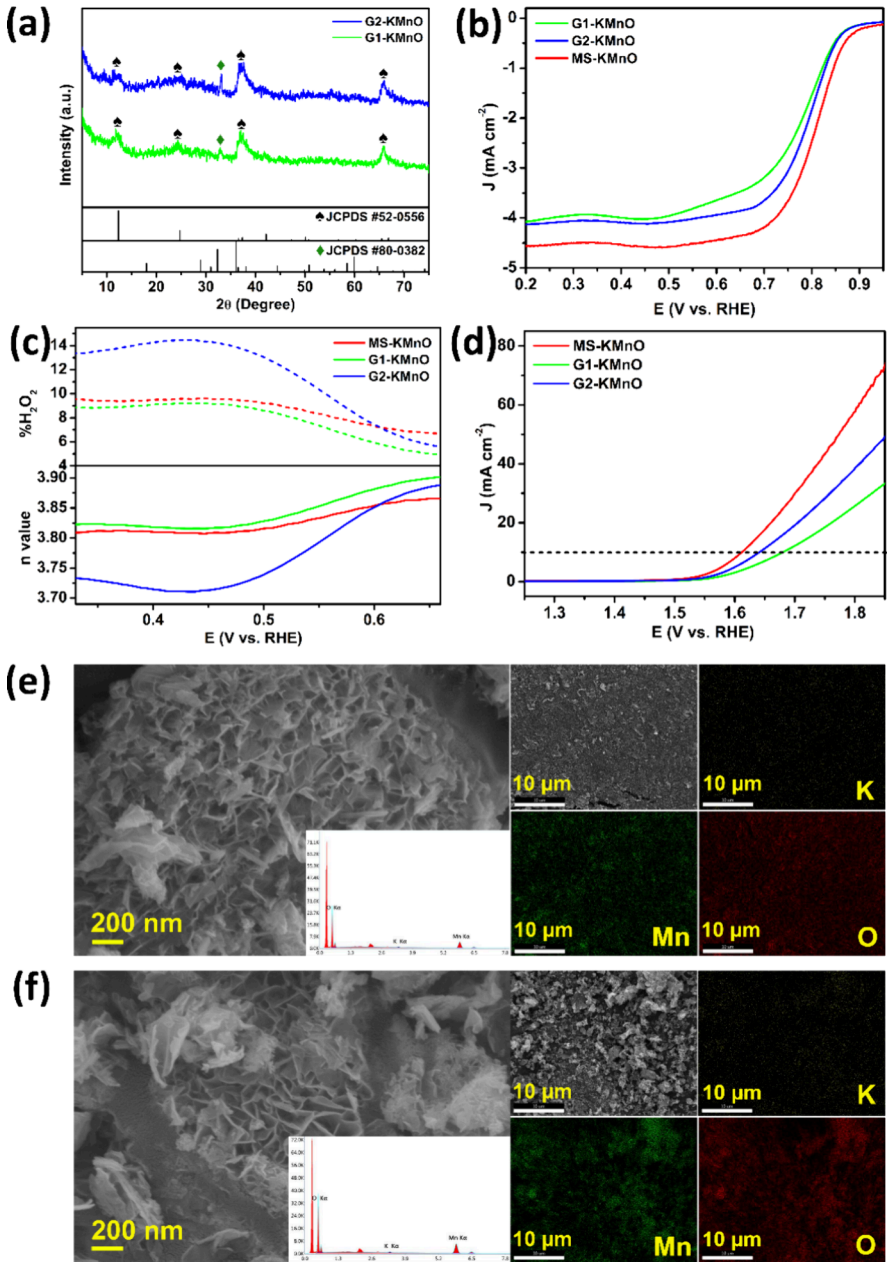

Figure 4. (a) XRD patterns, (b) ORR polarization curves, and (c) %H_2O_2 and n values as calculated from the RRDE curves. (d) OER polarization curves for MS-KMnO, G1-KMnO, and G2-KMnO. FESEM images at two different magnifications along with the EDS spectrum and elemental mapping for (e) G1-KMnO and (f) G2-KMnO.

isotherms. The curves showed a type-IV isotherm with a type-H3 hysteresis loop, suggesting a mesoporous structure and slit-shaped pores (Figure S12). The BET surface area, pore volume, and average pore size are given in Table S5. The surface area for MS-KMnO was substantially higher at 102.341 $m^2\ g^{-1}$, than that of Co-KMnO at 63.017 $m^2\ g^{-1}$. Although previous studies showed an increase in surface area on cobalt doping, in the present case, the type-II secondary structure development in Co-KMnO as discussed above may be the reason for the observed reduction in surface area and catalytic activity.[35,51]

To study the evolution of the type-II secondary morphology in Co-KMnO and its effect on activity, Co-doped samples were prepared at two lower temperatures, 360 and 370 °C, keeping all other parameters constant. The XRD patterns for Co-KMnO/360 and Co-KMnO/370 in Figure S7 show the formation of the birnessite phase even at lower temperatures. The SEM morphologies of Co-KMnO/360 and Co-KMnO/370 in Figure 5d,e show that the type-II secondary structure is limited to smaller patches, unlike Co-KMnO (Figure S9b). This disordered morphology may be due to lower reaction temperatures. The LSV curves for Co-KMnO/370 and Co-KMnO/360 toward ORR (Figure 5a) showed E_{onset} and $E_{1/2}$ at 0.85, 0.75 V, and 0.86, 0.76 V, respectively, which showed their enhanced activity in comparison to Co-KMnO. The OER activities of Co-KMnO/370 and Co-KMnO/360 in Figure 5b also follow a similar pattern, with their $E_{j=10}$ being 1.65 and 1.67 V, respectively. However, the bifunctional activity of MS-KMnO is still better than that of lower-temperature Co-doped samples.

https://doi.org/10.1021/acsomega.4c05500
ACS Omega 2025, 10, 4248−4260

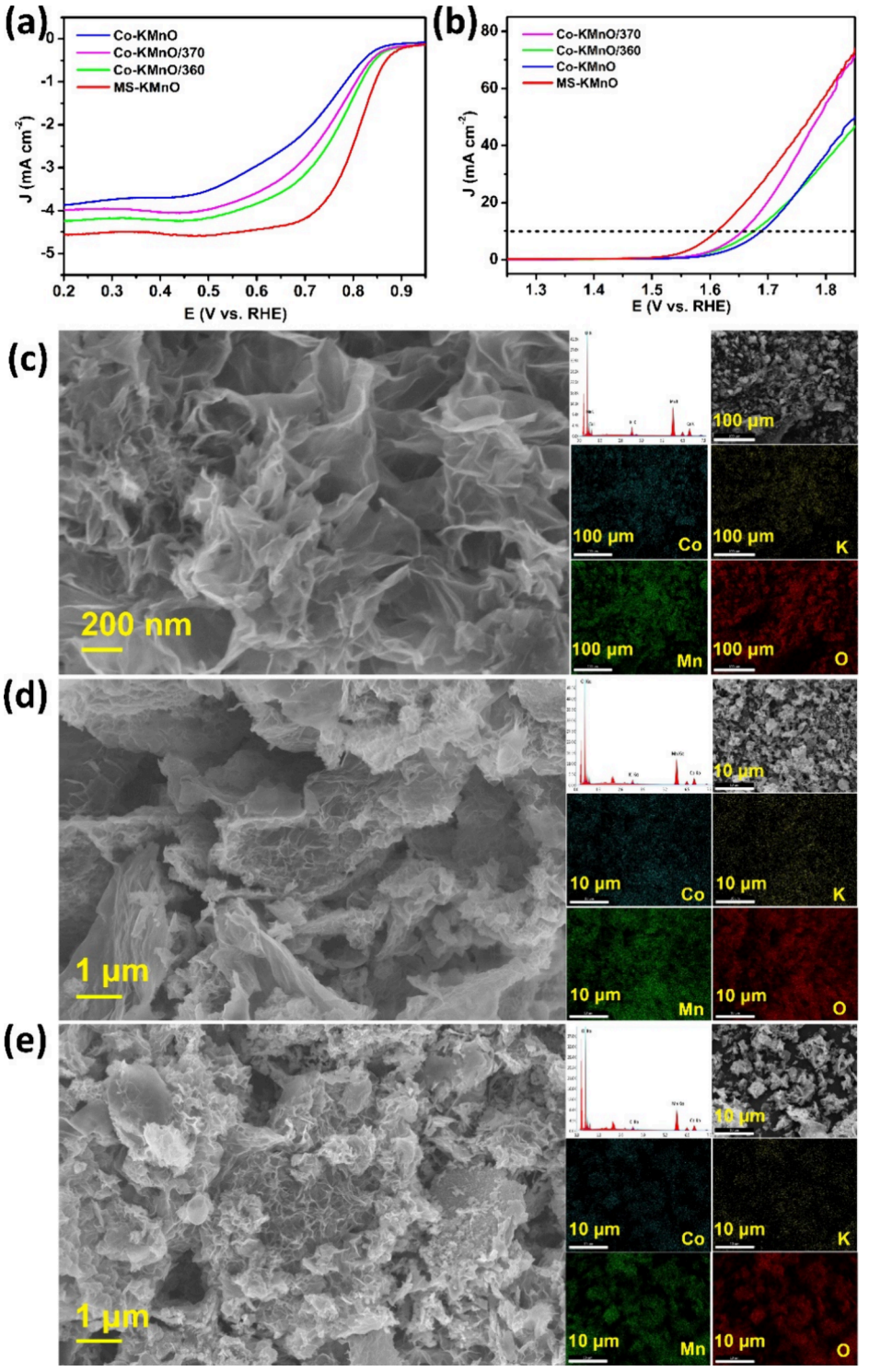

Figure 5. (a) ORR polarization curves and (b) OER polarization curves for Co-KMnO, Co-KMnO/370, Co-KMnO/360, and MS-KMnO, respectively. FESEM images at two different magnifications along with EDS spectrum and elemental mapping for (c) Co-KMnO, (d) Co-KMnO/370, and (e) Co-KMnO/360.

XPS analyses for MS-KMnO and Co-KMnO were carried out to understand the change in the surface composition on doping. The stoichiometric formulas calculated from the survey scan (Figures S13 and S14) are $K_{0.12}MnO_2{\cdot}0.51H_2O$ and $K_{0.2}Co_{0.35}MnO_2{\cdot}H_2O$, respectively. The Mn 2p core level spectra for MS-KMnO and Co-KMnO in Figure 6a,b show two distinct peaks due to Mn $2p_{1/2}$ and Mn $2p_{3/2}$. The higher energy Mn $2p_{3/2}$ peaks for MS-KMnO and Co-KMnO are observed at 642.26 and 642.5 eV, respectively. The higher Mn $2p_{3/2}$ binding energy in the case of Co-KMnO implies an increased contribution of Mn with higher oxidation states. The deconvolution of the Mn $2p_{3/2}$ and $2p_{1/2}$ peaks revealed the amount of different Mn oxidation states in each sample. The peaks at 640.30, 641.89, 643.09, and 645.99 correspond to Mn^{2+}, Mn^{3+}, Mn^{4+}, and shakeup peaks, respectively.[30,32,52,53] The Mn^{3+}/Mn^{4+} ratios for MS-KMnO and Co-KMnO were

https://doi.org/10.1021/acsomega.4c05500
ACS Omega 2025, 10, 4248−4260

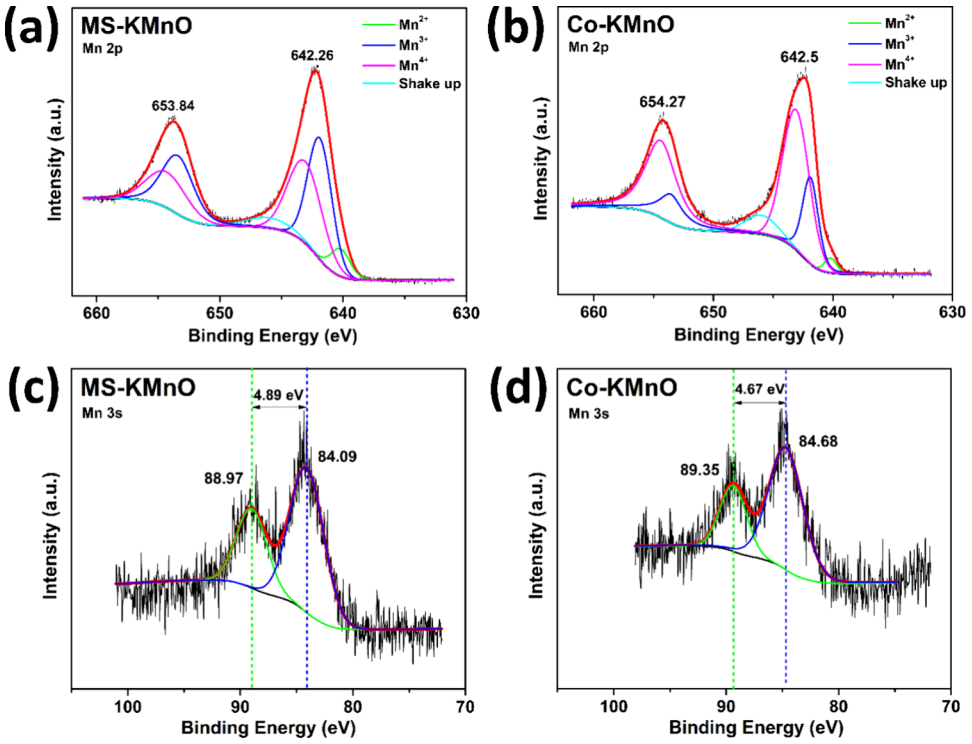

Figure 6. XPS spectra for MS-KMnO and Co-KMnO showing deconvoluted (a, b) Mn 2p and (c, d) Mn 3s regions, respectively.

Table 1. Mn^{3+}/Mn^{4+} Ratio Comparison between Previously Reported Studies and the Current Study

sl. no.	samples	atomic ratio (Co/Mn)	Mn^{3+}/Mn^{4+} in pristine birnessite	$\eta_{pristine}$ (mV)	Mn^{3+}/Mn^{4+} in Co-birnessite	$\eta_{Co\text{-}doped}$ (mV)	application	ref
1	$K_{0.01}[Co_{0.30}Mn_{0.70}O_2]$	0.43	0.28	780	0.11	425	OER	25
2	co-substituted birnessite	0.42	0.29	770	0.05	490	OER	35
3	Co^{2+}/birnessite	0.41	0.29	770	0.33	360	OER	35
4	Co-MnO_2 Co-KMnO	0.36	0.32 ΔE_{onset} = 287 mV	>570	0.4	430	OER ORR	51
5	$(K_{0.20}Co_{0.35}MnO_{3.04})$	0.35	1.19 (±0.005) ΔE_{onset} = 50 mV	400	0.37 (±0.0004)	500	OER ORR	(*this Work)

calculated to be 1.19 and 0.37, respectively. In the case of Co-KMnO, the concentration of Mn^{3+} decreased significantly, along with a decrease in the overall intensity of its peak, suggesting an effective replacement of Mn by Co ions. Moreover, the Co 2p spectrum for Co-KMnO at binding energies of 780.5 and 795.7 eV showed the presence of Co^{3+} ions (Figure S15).[54] The Mn 3s spectra in Figure 6c,d for MS-KMnO and Co-KMnO display Mn 3s orbital splitting energies of 4.89 and 4.67 eV, corresponding to Mn average oxidation states (AOSs) of 3.4 and 3.7, respectively. This indicates that the AOS value of Mn increases on Co doping. The replacement of Mn^{3+} by Co^{3+} in the MnO_2 lattice is the driving factor for the observed decrease in the value of Mn^{3+}/Mn^{4+}.

Table 1 summarizes the Co content and Mn^{3+}/Mn^{4+} in birnessite-based samples from the previously published literature in comparison with that of the present study.[25,35,51] The studies in Sl No. 1 and 2 reported that pristine birnessites have higher Mn^{3+}/Mn^{4+} ratios than their Co-doped counterparts. However, the studies in Sl No. 3 and 4 showed that the Co-doped birnessites have higher Mn^{3+}/Mn^{4+} ratios than the pristine ones. Irrespective of the variation in Mn^{3+}/Mn^{4+}, all of the above studies reported enhancement in the OER activity on Co doping. Therefore, in the case of doping studies in birnessite, the Mn^{3+}/Mn^{4+} ratio may not be taken as an activity descriptor. This leads to the understanding that although in the present study the Mn^{3+}/Mn^{4+} ratio decreases on doping, this may not be the deciding factor for the observed decrease in activity.

The stability of MS-KMnO at three different ORR potentials, 0.81 ($E_{1/2}$), 0.73 (before current saturation), and 0.54 V (after current saturation), was monitored by chronoamperometry (inset of Figure 1b). At 0.81 V, following an initial loss, a current plateau was observed up to 8000 s, and the current reached 78% of its initial value at 15,000 s. In contrast, at 0.73 and 0.54 V, the current decreased continuously with time and after 15,000 s, the current dropped to 67 and 49% of its initial values, respectively. These results show that the ORR stability depends on the applied potential, and activity degradation is accelerated at higher cathodic potentials. The LSV curves (Figure S16) taken before as well as after chronoamperometric studies for different potentials also corroborate the above observation. The ORR stability has also been monitored by continuously taking 1000 CV cycles in the ORR potential range (Figure S17a). The two samples recovered after chronoamperometry at 0.81 V and 1000 CV

https://doi.org/10.1021/acsomega.4c05500
ACS Omega 2025, 10, 4248−4260

cycles were characterized by SEM and XPS. The SEM micrographs obtained post chronoamperometry (Figure S18a−c) as well as post CV cycles (Figure S18d−f) show the development of secondary structures. The Mn 2p XPS spectra obtained post chronoamperometry (Figure S19a) and post CV (Figure S19b) were deconvoluted, and the Mn^{3+}/Mn^{4+} ratios were found to be 0.39 and 0.08, respectively. The analysis of post-ORR samples showed that during the ORR process, the MS-KMnO catalyst changes to decrease the Mn^{3+}/Mn^{4+} ratio and form the secondary morphology. This observation gives more insights into the ORR mechanism on MnO_2. The ORR process starts with the reductive adsorption of molecular oxygen on the active surface Mn^{3+} sites by the replacement of surface-adsorbed hydroxyl groups. In four reduction steps, adsorbed O_2 converts to superoxide (O_2^{2-}), (OOH^-) peroxide, and oxide (O^{2-}) consecutively, while the active site shuttles between Mn^{3+} and Mn^{4+}.[55] We propose that during the ORR process, the $Mn^{4+}-O^{2-}$ intermediate reacts with the surface Mn^{4+} of an adjacent flake in contact to form the $Mn^{4+}-O^{2-}-Mn^{4+}$ linkage to form secondary structures. This linkage does not allow Mn^{4+} to leave the oxide moiety and shuttle back to the Mn^{3+} state. This also explains the observed decrease in Mn^{3+}/Mn^{4+} on the post-ORR sample.

Furthermore, the stability of MS-KMnO (Ni foam) is investigated by chronopotentiometry at a constant OER current density of 50 mA/cm^2 for an operational period of 100 h (inset of Figure 1e). The small fluctuations in potential could be due to blocking of the electrode surface by the evolved oxygen gas. There is a gradual increase in potential at an overall rate of ∼2.7 mV h^{-1} with the final 40 h showing a slightly higher rate of degradation (3.5 mV h^{-1}) to reach an end potential of 1.89 V. The crystal structure and morphology of MS-KMnO after 100 h of chronopotentiometry were studied by ex situ XRD and FESEM analyses. The XRD pattern of post-treated MS-KMnO (Figure S20a) only shows a broad hump centered around 3.6 Å, in which the characteristic (003), (012), and (110) peaks of layered birnessite phase are absent. The ex situ SEM image (Figure S20b) shows perforated flakes of lateral size ranging from 50 to 100 nm. These investigations showed that after 100 h OER, there is degradation of both the crystal structure and the morphology of MS-KMnO, leading to the observed increase in potential. MS-KMnO is further subjected to 1000 CV cycles in the OER potential window (Figure S17b), and the post-treated sample is characterized by SEM and XPS ex situ. The SEM micrograph of the post-treated sample (Figure S21a−c) shows the development of the secondary structure, and the deconvoluted Mn 2p XPS spectrum (Figure S21d) shows a considerable decrease in Mn^{3+}/Mn^{4+} to 0.24. The enhanced OER activity of MS-KMnO is attributed to its primary morphology with exposed edge sites. Furthermore, the lower OER Tafel slope of MS-KMnO (53 mV dec^{-1}) implies better reaction kinetics and efficient use of applied potential and suggests the lattice oxygen oxidation mechanism (LOM) for the OER.[28,56,57] Through the LOM mechanism, MS-KMnO underwent lattice oxygen loss, resulting in structural and morphological degradation, which led to an increase in the applied potential for a steady current.

Previous studies also corroborate the fact that in MnO_x samples the surface Mn^{3+}/Mn^{4+} value decreases on ORR and OER.[58−61] In both ORR and OER mechanisms, it has been suggested that during the catalytic cycles, the Mn^{3+} active site undergoes a redox change with formation of different intermediate Mn−O species. However, the involvement of the lattice oxygen in the OER or incomplete cycling with peroxide generation during ORR leads to the formation of Mn^{4+} species at the expense of Mn^{3+}, resulting in the rapid degradation of the catalyst. Further studies may help in the development of strategies to stabilize these active Mn^{3+} species during oxygen electrolysis.

4. CONCLUSIONS

2D layered birnessite was prepared by different methods, exhibiting various morphologies. While the primary free-standing flake-like structure was formed by a molten salt method, the type-I secondary hierarchical honeycomb structure was formed by both hydrothermal and solution methods, and a thick plate-like structure was formed by the sol−gel method. The primary morphology of MS-KMnO prepared by the molten salt method provides the highest BET surface area (102.341 $m^2\ g^{-1}$), C_{dl} value (13.53 mF cm^{-2}), and Mn^{3+}/Mn^{4+} ratio (1.19). This is attributed to the enhanced bifunctional activity of MS-KMnO: ORR: E_{onset}, $E_{1/2}$, and Tafel slope at 0.89 V, 0.81 V, and 98 mV dec^{-1} respectively; OER: $E_{j=10}$ and Tafel slope at 1.53 V and 61 mV dec^{-1}, respectively. Modification of the molten salt method only to the extent of glucose addition led to the heat-induced evolution of the secondary structure and degradation of bifunctional activity. On the other hand, the addition of the cobalt precursor in the molten salt method led to Co^{3+} doping both in the in-layer and interlayer. The formation of a type-II secondary structure and reduction of the Mn^{3+}/Mn^{4+} ratio to 0.37 in Co-KMnO resulted in the lowering of the bifunctional activity. The amount of activity retention and stability of MS-KMnO to different electrochemical treatments were studied. The chronoamperometric study showed that the measured ORR current decreases on treatment at higher cathodic potentials. The post-treated sample showed the development of secondary structures along with a substantial decrease in the Mn^{3+}/Mn^{4+} ratio. On OER at a constant current of 50 mA cm^{-2} for a prolonged duration of 100 h, the sample showed morphological degradation to smaller perforated flakes with changes in the layered crystal structure. This study classified different morphologies within the birnessite polymorph, which is one of the decisive factors for tuning the bifunctional activity.

■ ASSOCIATED CONTENT

Supporting Information

The following files are available free of charge. The Supporting Information is available free of charge at https://pubs.acs.org/doi/10.1021/acsomega.4c05500.

Potential calibration of the Ag/AgCl reference electrode; CV curves for MS-KMnO, MKZ-KMnO, SG-KMnO, and HT-KMnO; RRDE curves for MS-KMnO, MKZ-KMnO, HT-KMnO, and SG-KMnO; LSV curves for MS-KMnO before as well as after chronoamperometry; CV curves in the nonfaradaic region and C_{dl} plots for the samples MS-KMnO, MKZ-KMnO, HT-KMnO, and SG-KMnO; RRDE plots for MS-KMnO, G1-KMnO, and G2-KMnO; XRD patterns of MS-KMnO, Co-KMnO, Co-KMnO/370, and Co-KMnO/360; RRDE plots for MS-KMnO and Co-KMnO; FESEM images of MS-KMnO and Co-KMnO; CV curves in the nonfaradaic region and C_{dl} plots of Co-KMnO; EIS plots of MS-

https://doi.org/10.1021/acsomega.4c05500
ACS Omega 2025, 10, 4248−4260

KMnO and Co-KMnO; N_2 adsorption−desorption isotherms of MS-KMnO and Co-KMnO; XPS survey spectra of MS-KMnO; XPS survey spectra of Co-KMnO; XPS Co 2p spectra of Co-KMnO; SEM images at different magnifications of MS-KMnO after the chronoamperometry test, 1000 CV cycles for ORR and 1000 CV cycles for OER; XPS Mn 2p spectra after chronoamperometry; XPS Mn 2p spectra after 1000 CV cycles for ORR; XPS Mn 2p spectra after 1000 CV cycles for OER (PDF)

AUTHOR INFORMATION

Corresponding Author

Kumar S. K. Varadwaj − *Department of Chemistry, Ravenshaw University, Cuttack, Odisha 753003, India;* orcid.org/0000-0003-3314-7677; Email: skvaradwaj@ravenshawuniversity.ac.in, svaradwaj@gmail.com

Authors

Rajesh K. Behera − *Department of Chemistry, Ravenshaw University, Cuttack, Odisha 753003, India*

Alaka P. Sahoo − *Department of Chemistry, Ravenshaw University, Cuttack, Odisha 753003, India*

Debidutta Das − *Department of Chemistry, Ravenshaw University, Cuttack, Odisha 753003, India*

Amarendra Nayak − *Department of Chemistry, Ravenshaw University, Cuttack, Odisha 753003, India*

Sikha Sayantani − *Department of Chemistry, Ravenshaw University, Cuttack, Odisha 753003, India*

Debasis Jena − *Department of Chemistry, Ravenshaw University, Cuttack, Odisha 753003, India;* orcid.org/0000-0002-4620-1225

Swarna P. Mantry − *School of Applied Sciences, Chandigarh University, Lucknow 209859, India*

Complete contact information is available at: https://pubs.acs.org/10.1021/acsomega.4c05500

Author Contributions

This manuscript was written through contributions of all authors. All authors have given approval to the final version of the manuscript. R.K.B. and A.P.S. contributed equally.

Notes

The authors declare no competing financial interest.

ACKNOWLEDGMENTS

This work was supported by the Center of Excellence in Environment and Public Health by Higher Education Department, Government of Odisha [Grant No.: 26913/HED/HE-PTC-WB-02-17] and S&T, Government of Odisha, Sanction No. 27562800512017. We acknowledge Malaya Kumar Sahoo, NISER, Bhubaneswar, for BET analysis, ICT-IOC, Bhubaneswar, for HRTEM, and IIT Kanpur for XPS analysis.

REFERENCES

(1) Lang, P.; Yuan, N.; Jiang, Q.; Zhang, Y.; Tang, J. Recent Advances and Prospects of Metal-based Catalysts for Oxygen Reduction Reaction. *Energy Technol.* **2020**, *8* (3), No. 1900984.

(2) Jaiswal, K. K.; Chowdhury, C. R.; Yadav, D.; Verma, R.; Dutta, S.; Jaiswal, K. S.; Karuppasamy, K. S. K. Renewable and Sustainable Clean Energy Development and Impact on Social, Economic, and Environmental Health. *Energy Nexus* **2022**, *7*, No. 100118.

(3) Rai, V.; Lee, K. P.; Safanama, D.; Adams, S.; Blackwood, D. J. Oxygen Reduction and Evolution Reaction (ORR and OER) Bifunctional Electrocatalyst Operating in a Wide PH Range for Cathodic Application in Li−Air Batteries. *ACS Appl. Energy Mater.* **2020**, *3* (9), 9417−9427.

(4) Singh, R. S.; Gautam, A.; Rai, V. Graphene-Based Bipolar Plates for Polymer Electrolyte Membrane Fuel Cells. *Front Mater. Sci.* **2019**, *13* (3), 217−241.

(5) Ruth, J. D.; Hayes, L. M.; Martin, D. R.; Hatipoglu, K. An Overview of Photoelectrochemical Cells (PEC): Mimicking Nature to Produce Hydrogen for Fuel Cells. In *SoutheastCon*; IEEE, 2017.

(6) Jiao, Y.; Zheng, Y.; Jaroniec, M.; Qiao, S. Z. Design of Electrocatalysts for Oxygen-and Hydrogen-Involving Energy Conversion Reactions. *Chem. Soc. Rev.* **2015**, *44* (8), 2060−2086.

(7) Tahir, M.; Pan, L.; Idrees, F.; Zhang, X.; Wang, L.; Zou, J.-J.; Wang, Z. L. Electrocatalytic Oxygen Evolution Reaction for Energy Conversion and Storage: A Comprehensive Review. *Nano Energy* **2017**, *37*, 136−157.

(8) Debe, M. K. Electrocatalyst Approaches and Challenges for Automotive Fuel Cells. *Nature* **2012**, *486* (7401), 43−51.

(9) Lee, J.; Jeong, B.; Ocon, J. D. Oxygen Electrocatalysis in Chemical Energy Conversion and Storage Technologies. *Curr. Appl. Phys.* **2013**, *13* (2), 309−321.

(10) Cherevko, S.; Geiger, S.; Kasian, O.; Kulyk, N.; Grote, J.-P.; Savan, A.; Shrestha, B. R.; Merzlikin, S.; Breitbach, B.; Ludwig, A. Oxygen and Hydrogen Evolution Reactions on Ru, RuO2, Ir, and IrO2 Thin Film Electrodes in Acidic and Alkaline Electrolytes: A Comparative Study on Activity and Stability. *Catal. Today* **2016**, *262*, 170−180.

(11) Cruz-Martínez, H.; Rojas-Chávez, H.; Matadamas-Ortiz, P. T.; Ortiz-Herrera, J. C.; López-Chávez, E.; Solorza-Feria, O.; Medina, D. I. Current Progress of Pt-Based ORR Electrocatalysts for PEMFCs: An Integrated View Combining Theory and Experiment. *Materials Today Physics* **2021**, *19*, No. 100406.

(12) Zeng, K.; Zheng, X.; Li, C.; Yan, J.; Tian, J.; Jin, C.; Strasser, P.; Yang, R. Recent Advances in Non-noble Bifunctional Oxygen Electrocatalysts toward Large-scale Production. *Adv. Funct Mater.* **2020**, *30* (27), No. 2000503.

(13) Mosa, I. M.; Biswas, S.; El-Sawy, A. M.; Botu, V.; Guild, C.; Song, W.; Ramprasad, R.; Rusling, J. F.; Suib, S. L. Tunable Mesoporous Manganese Oxide for High Performance Oxygen Reduction and Evolution Reactions. *J. Mater. Chem. A Mater.* **2016**, *4* (2), 620−631.

(14) Shao, Z.; Wu, X.; Wu, X.; Feng, S.; Huang, K. The Synthesis and Advantages of Spinel-Type Composites. *Mater. Chem. Front.* **2023**, *7*, 5288−5308.

(15) He, G.; Liao, Y. Modification of Micro/Nanoscaled Manganese Dioxide-Based Materials and Their Electrocatalytic Applications toward Oxygen Evolution Reaction. *J. Mater. Chem. A Mater.* **2023**, *11* (13), 6688−6746.

(16) Wang, P.; Zhang, S.; Wang, Z.; Mo, Y.; Luo, X.; Yang, F.; Lv, M.; Li, Z.; Liu, X. Manganese-Based Oxide Electrocatalysts for the Oxygen Evolution Reaction: A Review. *J. Mater. Chem. A Mater.* **2023**, *11* (11), 5476−5494.

(17) Paul, S.; Neese, F.; Pantazis, D. A. Structural Models of the Biological Oxygen-Evolving Complex: Achievements, Insights, and Challenges for Biomimicry. *Green Chem.* **2017**, *19* (10), 2309−2325.

(18) Zhang, C.; Chen, C.; Dong, H.; Shen, J.-R.; Dau, H.; Zhao, J. A Synthetic Mn4Ca-Cluster Mimicking the Oxygen-Evolving Center of Photosynthesis. *Science (1979)* **2015**, *348* (6235), 690−693.

(19) Meng, Y.; Song, W.; Huang, H.; Ren, Z.; Chen, S.-Y.; Suib, S. L. Structure−Property Relationship of Bifunctional MnO2 Nanostructures: Highly Efficient, Ultra-Stable Electrochemical Water Oxidation and Oxygen Reduction Reaction Catalysts Identified in Alkaline Media. *J. Am. Chem. Soc.* **2014**, *136* (32), 11452−11464.

(20) Xiao, W.; Wang, D.; Lou, X. W. Shape-Controlled Synthesis of MnO2 Nanostructures with Enhanced Electrocatalytic Activity for Oxygen Reduction. *J. Phys. Chem. C* **2010**, *114* (3), 1694−1700.

(21) Zhou, Z.; Zheng, X.; Huang, H.; Wu, Y.; Han, S.; Cai, W.; Lan, B.; Sun, M.; Yu, L. The Synergistically Enhanced Activity and Stability of Layered Manganese Oxide via the Engineering of Defects and K+

Ions for Oxygen Electrocatalysis. *CrystEngComm* **2022**, *24* (12), 2327−2335.
(22) Hu, Z.; Chen, M.; Zhang, H.; Huang, L.; Liu, K.; Ling, Y.; Zhou, H.; Jiang, Z.; Feng, G.; Zhou, J. Stabilization of Layered Manganese Oxide by Substitutional Cation Doping. *J. Mater. Chem. A Mater.* **2019**, *7* (12), 7118−7127.
(23) Hou, J.; Li, Y.; Mao, M.; Ren, L.; Zhao, X. Tremendous Effect of the Morphology of Birnessite-Type Manganese Oxide Nanostructures on Catalytic Activity. *ACS Appl. Mater. Interfaces* **2014**, *6* (17), 14981−14987.
(24) Thenuwara, A. C.; Shumlas, S. L.; Attanayake, N. H.; Cerkez, E. B.; McKendry, I. G.; Frazer, L.; Borguet, E.; Kang, Q.; Zdilla, M. J.; Sun, J. Copper-Intercalated Birnessite as a Water Oxidation Catalyst. *Langmuir* **2015**, *31* (46), 12807−12813.
(25) McKendry, I. G.; Thenuwara, A. C.; Shumlas, S. L.; Peng, H.; Aulin, Y. V.; Chinnam, P. R.; Borguet, E.; Strongin, D. R.; Zdilla, M. J. Systematic Doping of Cobalt into Layered Manganese Oxide Sheets Substantially Enhances Water Oxidation Catalysis. *Inorg. Chem.* **2018**, *57* (2), 557−564.
(26) McKendry, I. G.; Mohamad, L. J.; Thenuwara, A. C.; Marshall, T.; Borguet, E.; Strongin, D. R.; Zdilla, M. J. Synergistic In-Layer Cobalt Doping and Interlayer Iron Intercalation into Layered MnO2 Produces an Efficient Water Oxidation Electrocatalyst. *ACS Energy Lett.* **2018**, *3* (9), 2280−2285.
(27) Frey, C. E.; Wiechen, M.; Kurz, P. Water-Oxidation Catalysis by Synthetic Manganese Oxides−Systematic Variations of the Calcium Birnessite Theme. *Dalton transactions* **2014**, *43* (11), 4370−4379.
(28) Ju, M.; Chen, Z.; Zhu, H.; Cai, R.; Lin, Z.; Chen, Y.; Wang, Y.; Gao, J.; Long, X.; Yang, S. Fe (III) Docking-Activated Sites in Layered Birnessite for Efficient Water Oxidation. *J. Am. Chem. Soc.* **2023**, *145* (20), 11215−11226.
(29) Chen, Z.; Ju, M.; Sun, M.; Jin, L.; Cai, R.; Wang, Z.; Dong, L.; Peng, L.; Long, X.; Huang, B. TM LDH Meets Birnessite: A 2D-2D Hybrid Catalyst with Long-Term Stability for Water Oxidation at Industrial Operating Conditions. *Angew. Chem., Int. Ed.* **2021**, *60* (17), 9699−9705.
(30) Sun, S.; Xue, Y.; Wang, Q.; Huang, H.; Miao, H.; Liu, Z. Cerium Ion Intercalated MnO2 Nanospheres with High Catalytic Activity toward Oxygen Reduction Reaction for Aluminum-Air Batteries. *Electrochim. Acta* **2018**, *263*, 544−554.
(31) Kosasang, S.; Ma, N.; Wuamprakhon, P.; Phattharasupakun, N.; Maihom, T.; Limtrakul, J.; Sawangphruk, M. Insight into the Effect of Intercalated Alkaline Cations of Layered Manganese Oxides on the Oxygen Reduction Reaction and Oxygen Evolution Reaction. *Chem. Commun.* **2018**, *54* (62), 8575−8578.
(32) Mantry, S. P.; Mohapatra, B. D.; Behera, N.; Mishra, P.; Parhi, P.; Varadwaj, K. S. K. Potentiostatic Regeneration of Oxygen Reduction Activity in MnOx@ Graphene Hybrid Nanostructures. *Electrochim. Acta* **2019**, *325*, No. 134947.
(33) Ochirkhuyag, A.; Varga, T.; Tóth, I. Y.; Varga, Á. T.; Sápi, A.; Kukovecz, A.; Kónya, Z. Cost-Effective Ion-Tuning of Birnessite Structures for Efficient ORR Electrocatalysts. *Int. J. Hydrogen Energy* **2020**, *45* (32), 16266−16276.
(34) Sun, S.; Miao, H.; Xue, Y.; Wang, Q.; Zhang, Q.; Dong, Z.; Li, S.; Huang, H.; Liu, Z. High Electrocatalytic Activity of Silver-Doped Manganese Dioxide toward Oxygen Reduction Reaction in Aluminum-Air Battery. *J. Electrochem. Soc.* **2017**, *164* (7), F768.
(35) Thenuwara, A. C.; Shumlas, S. L.; Attanayake, N. H.; Aulin, Y. V.; McKendry, I. G.; Qiao, Q.; Zhu, Y.; Borguet, E.; Zdilla, M. J.; Strongin, D. R. Intercalation of Cobalt into the Interlayer of Birnessite Improves Oxygen Evolution Catalysis. *ACS Catal.* **2016**, *6* (11), 7739−7743.
(36) Thenuwara, A. C.; Cerkez, E. B.; Shumlas, S. L.; Attanayake, N. H.; McKendry, I. G.; Frazer, L.; Borguet, E.; Kang, Q.; Remsing, R. C.; Klein, M. L. Nickel Confined in the Interlayer Region of Birnessite: An Active Electrocatalyst for Water Oxidation. *Angew. Chem., Int. Ed.* **2016**, *128* (35), 10537−10541.
(37) Mathur, A.; Kumari, S.; Singh, A.; Mitra, R.; Sharma, R.; Biswas, K.; Halder, A. Surface Engineering of 2D Layered MnO2 with Co-Doping of Ni and Fe for Rechargeable Zinc-Air Battery. *J. Energy Storage* **2023**, *74*, No. 109350.
(38) Takashima, T.; Hashimoto, K.; Nakamura, R. Mechanisms of PH-Dependent Activity for Water Oxidation to Molecular Oxygen by MnO2 Electrocatalysts. *J. Am. Chem. Soc.* **2012**, *134* (3), 1519−1527.
(39) Peng, H.; McKendry, I. G.; Ding, R.; Thenuwara, A. C.; Kang, Q.; Shumlas, S. L.; Strongin, D. R.; Zdilla, M. J.; Perdew, J. P. Redox Properties of Birnessite from a Defect Perspective. *Proc. Natl. Acad. Sci. U. S. A.* **2017**, *114* (36), 9523−9528.
(40) Remsing, R. C.; McKendry, I. G.; Strongin, D. R.; Klein, M. L.; Zdilla, M. J. Frustrated Solvation Structures Can Enhance Electron Transfer Rates. *J. Phys. Chem. Lett.* **2015**, *6* (23), 4804−4808.
(41) Bhullar, R. K.; Zdilla, M. J.; Klein, M. L.; Remsing, R. C. Effect of Water Frustration on Water Oxidation Catalysis in the Nanoconfined Interlayers of Layered Manganese Oxides Birnessite and Buserite. *J. Mater. Chem. A Mater.* **2021**, *9* (11), 6924−6932.
(42) Chen, Z.; Wang, Z.; Cai, R.; Xie, Y.; Yu, J.; Long, X.; Yang, B.; Yang, S. NiMn Compound Nanosheets for Electrocatalytic Water Oxidation: Effects of Atomic Structures and Oxidation States. *Nanoscale* **2020**, *12* (4), 2472−2478.
(43) Huynh, M.; Shi, C.; Billinge, S. J. L.; Nocera, D. G. Nature of Activated Manganese Oxide for Oxygen Evolution. *J. Am. Chem. Soc.* **2015**, *137* (47), 14887−14904.
(44) Li, Y.-F.; Liu, Z.-P. Active Site Revealed for Water Oxidation on Electrochemically Induced δ-MnO2: Role of Spinel-to-Layer Phase Transition. *J. Am. Chem. Soc.* **2018**, *140* (5), 1783−1792.
(45) He, S.; Ji, D.; Novello, P.; Li, X.; Liu, J. Partial Surface Oxidation of Manganese Oxides as an Effective Treatment to Improve Their Activity in Electrochemical Oxygen Reduction Reaction. *J. Phys. Chem. C* **2018**, *122* (37), 21366−21374.
(46) Ma, L.; Meng, N.; Zhang, Y.; Lian, F. Improved Electrocatalytic Activity of δ-MnO2@ MWCNTs by Inducing the Oriented Growth of Oxygen Reduction Products in Li-O2 Batteries. *Nano Energy* **2019**, *58*, 508−516.
(47) Liu, F.; Wang, L.; Yang, W.; Liu, E.; Huang, C. A Sandwich-Type Catalytic Composite Reassembled with a Birnessite Layer and Metalloporphyrin as a Water Oxidation Catalyst. *RSC Adv.* **2019**, *9* (13), 7440−7446.
(48) Kang, Q.; Vernisse, L.; Remsing, R. C.; Thenuwara, A. C.; Shumlas, S. L.; McKendry, I. G.; Klein, M. L.; Borguet, E.; Zdilla, M. J.; Strongin, D. R. Effect of Interlayer Spacing on the Activity of Layered Manganese Oxide Bilayer Catalysts for the Oxygen Evolution Reaction. *J. Am. Chem. Soc.* **2017**, *139* (5), 1863−1870.
(49) Ching, S.; Petrovay, D. J.; Jorgensen, M. L.; Suib, S. L. Sol−Gel Synthesis of Layered Birnessite-Type Manganese Oxides. *Inorg. Chem.* **1997**, *36* (5), 883−890.
(50) Galakhov, V. R.; Demeter, M.; Bartkowski, S.; Neumann, M.; Ovechkina, N. A.; Kurmaev, E. Z.; Lobachevskaya, N. I.; Mukovskii, Y. M.; Mitchell, J.; Ederer, D. L. Mn 3 s Exchange Splitting in Mixed-Valence Manganites. *Phys. Rev. B* **2002**, *65* (11), No. 113102.
(51) Chen, B.; Miao, H.; Hu, R.; Yin, M.; Wu, X.; Sun, S.; Wang, Q.; Li, S.; Yuan, J. Efficiently Optimizing the Oxygen Catalytic Properties of the Birnessite Type Manganese Dioxide for Zinc-Air Batteries. *J. Alloys Compd.* **2021**, *852*, No. 157012.
(52) Mantry, S. P.; Mohapatra, B. D.; Behera, R. K.; Varadwaj, K. S. K. Oxygen Reduction Activity of Fe/Co/Ni Doped MnOx@ Graphene Nanohybrid: A Comparative Study. *J. Electroanal. Chem.* **2022**, *904*, No. 115767.
(53) Tang, Q.; Jiang, L.; Liu, J.; Wang, S.; Sun, G. Effect of Surface Manganese Valence of Manganese Oxides on the Activity of the Oxygen Reduction Reaction in Alkaline Media. *ACS Catal.* **2014**, *4* (2), 457−463.
(54) Zhao, Y.; Zhang, J.; Wu, W.; Guo, X.; Xiong, P.; Liu, H.; Wang, G. Cobalt-Doped MnO2 Ultrathin Nanosheets with Abundant Oxygen Vacancies Supported on Functionalized Carbon Nanofibers for Efficient Oxygen Evolution. *Nano Energy* **2018**, *54*, 129−137.

https://doi.org/10.1021/acsomega.4c05500
ACS Omega 2025, 10, 4248−4260

(55) Suntivich, J.; Gasteiger, H. A.; Yabuuchi, N.; Nakanishi, H.; Goodenough, J. B.; Shao-Horn, Y. Design Principles for Oxygen-Reduction Activity on Perovskite Oxide Catalysts for Fuel Cells and Metal−Air Batteries. *Nat. Chem.* **2011**, *3* (7), 546−550.
(56) Dong, K.; Yao, Y.; Li, H.; Li, H.; Sun, S.; He, X.; Wang, Y.; Luo, Y.; Zheng, D.; Liu, Q.; Li, Q.; Ma, D.; Sun, X.; Tang, B. H2O2-Mediated Electrosynthesis of Nitrate from Air. *Nature Synthesis* **2024**, *3* (6), 763−773.
(57) Dong, K.; Xu, Z.; He, X.; Zhao, D.; Chen, H.; Liang, J.; Luo, Y.; Sun, S.; Zheng, D.; Liu, Q.; Alshehri, A. A.; Feng, Z.; Wang, Y.; Sun, X. Ultrathin Single-Crystal $PtSe_2$ Nanosheets for High-Efficiency O_2 Electroreduction to H_2O_2. *Chem. Commun.* **2022**, *58* (76), 10683−10686.
(58) Pei, Y.; Wilkinson, D. P.; Gyenge, E. Insights into the Electrochemical Behavior of Manganese Oxides as Catalysts for the Oxygen Reduction and Evolution Reactions: Monometallic Core-Shell Mn/Mn_3O_4. *Small* **2023**, *19* (19). .
(59) Bisen, O. Y.; Baumung, M.; Tatzel, M.; Volkert, C. A.; Risch, M. Manganese Dissolution in Alkaline Medium with and without Concurrent Oxygen Evolution in $LiMn_2O_4$. *Energy Advances* **2024**, *3* (2), 504−514.
(60) Dong, K.; Liang, J.; Wang, Y.; Xu, Z.; Liu, Q.; Luo, Y.; Li, T.; Li, L.; Shi, X.; Asiri, A. M.; Li, Q.; Ma, D.; Sun, X. Honeycomb Carbon Nanofibers: A Superhydrophilic O_2 -Entrapping Electrocatalyst Enables Ultrahigh Mass Activity for the Two-Electron Oxygen Reduction Reaction. *Angew. Chem., Int. Ed.* **2021**, *60* (19), 10583−10587.
(61) Dong, K.; Liang, J.; Wang, Y.; Ren, Y.; Xu, Z.; Zhou, H.; Li, L.; Liu, Q.; Luo, Y.; Li, T.; Asiri, A. M.; Li, Q.; Ma, D.; Sun, X. Plasma-Induced Defective TiO2-x with Oxygen Vacancies: A High-Active and Robust Bifunctional Catalyst toward H2O2 Electrosynthesis. *Chem. Catalysis* **2021**, *1* (7), 1437−1448.

https://doi.org/10.1021/acsomega.4c05500
ACS Omega 2025, 10, 4248−4260